

# An Implementation of Synthetic Aperture Focusing Technique in Frequency Domain

Tadeusz Stepinski, *Senior Member, IEEE*

**Abstract**—A new implementation of a synthetic aperture focusing technique (SAFT) based on concepts used in synthetic aperture radar and sonar is presented in the paper. The algorithm, based on the convolution model of the imaging system developed in frequency domain, accounts for the beam pattern of the finite-sized transducer used in the synthetic aperture. The 2D fast Fourier transform (FFT) is used for the calculation of a 2D spectrum of the ultrasonic data. The spectrum is then interpolated to convert the polar coordinate system used for the acquisition of ultrasonic signals to the rectangular coordinates used for the presentation of imaging results. After compensating the transducer lobe amplitude profile using a Wiener filter, the transformed spectrum is subjected to the 2D inverse Fourier transform to get the time-domain image again. The algorithm is computationally attractive due to the use of 2D FFT. The performance of the proposed frequency-domain algorithm and the classical time-domain SAFT are compared in the paper using simulated and real ultrasonic data.

## I. INTRODUCTION

ALTHOUGH advanced synthetic aperture focusing techniques (SAFT) implemented in frequency domain have been widely used for many years in radar (synthetic aperture radar, SAR) and sonar (synthetic aperture sonar, SAS), they are relatively unknown in medical applications and nondestructive evaluation (NDE) of materials. Only a simple time-domain SAFT (t-d SAFT) has been applied in NDE for detection and characterization of defects in thick metal structures, especially in nuclear power plants [1], [2].

In SAFT, the pulse-echo measurements made at a multitude of transmitter/receiver locations are combined to form a map of the ultrasonic reflectivity of the insonified region of interest (ROI). The method takes advantage of both spatial and temporal correlations to enhance the resolution and the signal-to-noise ratio of the resultant images. SAFT has been used in ultrasonic imaging systems mainly due to its two benefits: first, it is capable of improving lateral resolution in the focal zone, and second, it extends the focal zone resulting in a dynamic focusing effect [1], [2]. However, the performance of SAFT in practical applications, especially in the near field, depends on the particular implementation of the algorithm as well as on the size of the transducer used in synthetic aperture [3].

Usually, the NDE and medical SAFT implementations are performed using a delay-and-sum (DAS) processing

in time domain [4], [5]. DAS is a straightforward way of simulating the required lens effect commonly used in array beamformers. Such an implementation, while physically understandable, has been shown to be quite time consuming on general purpose computers due to a large number of parallel operations. Most SAFT implementations are based on a very simplified model of the imaging system used for developing radar and sonar applications. Such implementations can perform relatively well provided that the theoretical assumptions, generally valid for SAR and SAS, are fulfilled in the particular application. The principal assumption, which is usually correct in radar and sonar, is that the ROI is located in the far field of the transducer (antenna) used for creating synthetic array where its specific diffraction effects can be neglected (point-like source assumption). Unfortunately, this is not always valid in ultrasonic imaging, especially in the high-frequency NDE applications where the transducer is often in contact with the inspected structure. At least two kinds of problems may be encountered in such setup; first, the transducer's diffraction effects may impair image quality, and second, sparse spatial sampling used for gathering ultrasonic data may yield artifacts in the resulting image. Apparently, the analysis of SAFT performance for finite-sized transducers should be of great interest for its potential users.

Interestingly, judging from the literature, recent developments of advanced processing methods for high-resolution imaging in SAR and SAS (see, e.g., [6], [7]) have had no significant impact on the implementations of synthetic aperture imaging either in NDE or in medicine. It seems that the frequency-domain algorithms based on efficient fast Fourier transform (FFT) schemes have been developed for SAR and SAS applications, while, as already mentioned above, the NDE and medical applications have mostly relied on the time-domain DAS schemes. Although a number of authors have reported different implementations of frequency-domain SAFT, e.g., [8]–[13], the recently developed algorithms using the framework for SAR and SAS seem to be much less popular than the classical t-d SAFT implementations. This concerns especially the area of NDE where the development of new techniques lags after the fast progress of medical applications observed in the recent decennium.

One possible explanation might be that SAR and SAS have been developed by radar and communications specialists using specific radar terminology that obscured this technology to specialists in other fields. Another reason might be traditional differences between those fields; for

Manuscript received September 14, 2006; accepted March 7, 2007. Grateful acknowledgment is made to the Swedish Nuclear Fuel and Waste Management Co (SKB) for their support of this project.

The author is with Signals and Systems, Uppsala University, Uppsala, Sweden (e-mail: ts@angstrom.uu.se).

Digital Object Identifier 10.1109/TUFFC.2007.400

instance, in NDE systems the RF signals are sampled and processed directly in time domain, whereas in SAR and SAS the quadrature demodulation is performed before processing the complex valued baseband signals in frequency domain.

Accurate Fourier-based imaging techniques, developed recently in SAR, relate Fourier components of the measured SAR signal to the Fourier components of the target to be imaged. The origin of this approach can be found in the wave equation inversion theory, which is also known as wavefront reconstruction or holography [6], [14]. The basic principle behind wavefront reconstruction is the use of Fourier decomposition of the Green's function (also known as the spherical phase function), which represents the impulse response of an imaging system [6].

Digital implementations of the wavefront reconstruction for SAR rely on the discrete Fourier analysis of the SAR signal and the target function. The successful implementation of the advanced SAR multidimensional digital signal-processing algorithms requires a thorough understanding of SAR imaging as well as the resulting sampling constraints in both time and space. These issues do not pose serious problems for SAR specialists but may be quite unfamiliar to the designers of ultrasonic systems, especially in the field of NDE.

All digital implementations of SAFT require discretization of time and space and also transformation of polar coordinates, natural for ultrasonic transducers that integrate echoes arriving from the same distance, into Cartesian coordinates used for mapping the ROI. While responses of point targets in a transducer's far field are relatively straight and do not require dense mesh, the situation in the near field is quite different—the responses contain high spatial frequencies and require a dense mesh and an efficient interpolation when the respective coordinate systems are being transformed.

Accurate solutions to the wavefront reconstruction problem in a two-dimensional (2D) coordinate system are defined in terms of a space-variant and 2D operation that makes SAR processing a challenge. A number of schemes have been introduced that apply different approximations to circumvent the computational difficulties encountered; see [15] for review.

In the present paper we propose a frequency-domain SAFT algorithm, which is a modified version of the wavenumber ( $\omega$ - $k$ ) implementations known from SAR and SAS [6], [15], [16]. The algorithm is derived using a model developed in terms of wave equations. The model, which is valid in the far field, accounts for the beam pattern of a finite-sized transducer used in the synthetic aperture. As in the  $\omega$ - $k$  implementations, the proposed algorithm employs the 2D FFT for transforming data between the time and frequency domains, and a formal transform of the polar coordinate system, natural for ultrasonic transducers, to the Cartesian system used for the presentation of imaging results. However, since we intend to use the algorithm in the range interval where the point source assumption may be not valid, we introduce a filter for compensation

of the transducer beam pattern amplitude. We compare the performance of the proposed algorithm to that of the standard t-d SAFT based on DAS operations with emphasis on the lateral (cross-range) resolution. The resolution and the side lobes of the algorithms are compared in the analysis, and it is shown that the proposed algorithm consistently performs better than the standard t-d SAFT.

The paper is organized as follows: in the next section, we present theory starting from the basic relations defining the resolution and the sampling constraints that apply to the synthetic aperture setup. This presentation is followed by the models of the imaging system and the circular transducer that is used in the proposed algorithm. In the subsequent section, results of the simulations performed for the t-d SAFT and the proposed algorithm are presented and their performance is compared. Finally, we show experimental results obtained in a simple setup with wire targets immersed in water.

## II. THEORY

### A. Resolution and Spatial Sampling in SAFT

Below, we will define spatial resolution of a synthetic aperture in monostatic strip-map mode (i.e., a linear equally sampled aperture without transducer beam-steering), which is an appropriate setup in many ultrasonic applications.

There is an important difference between physical linear arrays and synthetic arrays, which results in the synthetic aperture having a resolution finer than that corresponding to the real linear array of the same length, focused in reception. Assuming that in a physical linear array the transmission results in an illumination of the ROI and the angle selectivity is performed in a receive beamformer, the differences in phase received by each element of the array contribute to its beam pattern. In the synthetic aperture, on the other hand, the same element radiates and receives signals and therefore the round-trip phase shift is effective in forming the resulting radiation pattern. As an important consequence of this fact, the synthetic aperture has two times finer lateral (cross-range) resolution for the same aperture length, which can be expressed as

$$\delta_{3\text{dB}} \cong \frac{R\lambda}{2L_{\text{eff}}}, \quad (1)$$

where  $\lambda$  is the wavelength and  $\delta_{3\text{dB}}$  is the effective half-power beamwidth of the synthetic aperture with length  $L_{\text{eff}}$  at a distance  $R$ , [17]. The parameter  $L_{\text{eff}}$  denotes an effective aperture length that is defined as the largest aperture length corresponding to  $\lambda$ , which contributes to the SAFT performance in terms of its lateral resolution. It is assumed that the signals received by all elements of a synthetic aperture are used efficiently if the  $L_{\text{eff}}$  is no longer than the half-power lobewidth of the transducer (element) used in the aperture. For a circular transducer with diameter  $d$ , the half-power lobewidth at a distance  $R$  will be

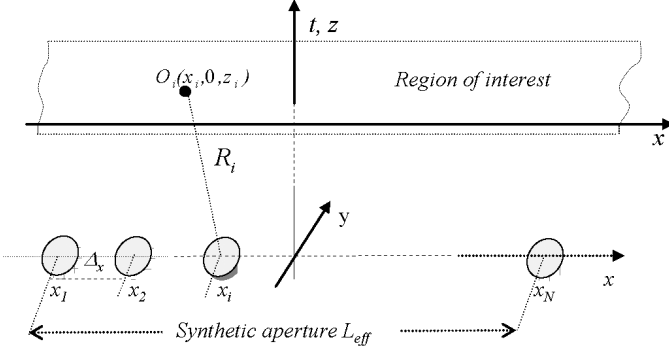


Fig. 1. Geometry of the synthetic aperture. At each position  $\{x_1, x_2, \dots, x_N\}$  of the synthetic aperture with length  $L_{\text{eff}}$ , the transducer emits a pulse and receives an echo from a number of targets located in the range  $R_i$  at the points  $O_i$ .

$$L_{\text{eff}} \cong \frac{R\lambda}{d}. \quad (2)$$

Inserting this expression into (1), we get the fundamental relation defining lateral resolution of synthetic aperture:

$$\delta_{3\text{dB}} \cong \frac{d}{2}. \quad (3)$$

Thus the resolution obtained from a synthetic aperture is independent of frequency and range if the effective aperture length is used. Analysis of the support band of the SA signal in the cross-range direction leads to the condition for spatial sampling step:

$$\Delta_x \leq \frac{R\lambda}{4L_{\text{eff}}}. \quad (4)$$

Eq. (4) reduces to  $\Delta_x \leq (d/4)$  if the effective aperture defined by (2) is used for the shortest wavelength represented in the ultrasonic pulse (see [17], [18] for details). Note that, in practical applications, the minimum transducer diameter  $d$  is limited by the minimal field intensity in the medium required for obtaining satisfactory signal-to-noise level in the receiver. The relations presented above are correct for a monochromatic wave and the targets located on the symmetry axis of the aperture.

### B. Model of the Imaging System

In this section we present a general model of an imaging system that will enable deriving the imaging algorithm. The model, which is derived here for circular sources, can easily be generalized to other transducer geometries (for instance, rectangular array elements).

Let us consider the synthetic aperture consisting of  $N$  transducer positions  $\{x_1, x_2, \dots, x_N\}$  in the setup shown in Fig. 1. The aperture is created when a single transducer (or an array) performs  $N$  pulse-echo measurements at the positions  $\{x_1, x_2, \dots, x_N\}$ , respectively. The transducer in its successive positions irradiates the ROI located in the  $xz$ -plane. At each position the transducer (or the respective array element) emits an acoustic wave and receives

an echo from an object defined by the reflectivity function  $f(x, y, z)$  (e.g., including a finite number of point targets at points  $O_i(x_i, 0, z_i)$ ). The successive transducer positions located along the  $x$ -axis in the rectangular coordinate system  $xz$  are spaced with the pitch  $\Delta_x$ . The transducer is excited by an electrical pulse  $e_i(t)$  and it receives in each respective location  $\{x_1, x_2, \dots, x_N\}$  the electrical signals  $s(x_k, t) \in \{s(x_1, t), s(x_2, t), \dots, s(x_N, t)\}$  that can be presented in the aggregated form referred to as B-scan image.

Our task is to perform imaging in a predefined ROI located in front of the synthetic aperture at the symmetry plane  $xz$ , using the signal set  $s(x_k, t)$ , and, in particular, to enhance the lateral resolution in this region.

Following the notation used in SAR, we will derive the imaging algorithm for a continuous time and space model based on a number of measurements in the discrete points along the axis  $x$ . For each transducer position  $x_k$ , the imaging model can be defined using the fundamental expression used for SAR imaging [15], [18]:

$$s(x_k, t) = \iint_{xz} f(x, z) \delta \left( t - \frac{2}{c} \sqrt{z^2 + (x - x_k)^2} \right) dz dx, \quad (5)$$

where  $x_k$  is transducer's position,  $f(x, z)$  denotes object's reflectivity function,  $c$  is sound velocity, and it is assumed that the transducer emits an impulse  $\delta(\cdot)$ .

Eq. (5) is valid assuming that the transducer diameter  $d$  is small compared to the wavelength  $\lambda$ ; in other words, the transducer can be regarded as a point source; that is, its specific diffraction effects as well as its electrical characteristics can be neglected. This implies that the response of a single point target takes the form of a single hyperbola in the B-scan, and the assumptions required for the standard SAFT based on the DAS operations are fulfilled. Below, we will present a more realistic transducer model, which includes the transducer's far-field beam pattern as well as its electrical frequency response.

### C. Transducer Model

Here, we will consider the case when a finite-sized transducer is used for the measurements and its diffraction pattern has to be taken into account. However, our analysis will be confined to the far-field zone where the Fraunhofer approximation can be used. We start by deriving an expression defining the signals  $s(x_k, t)$  for a single circular transducer. This expression will then be used for the derivation of the synthetic aperture scheme in frequency domain.

Let us consider a circular piston transducer of radius  $a$  in the polar coordinate system shown in Fig. 2. Since the same transducer is used for all the measurements, we introduce a separate coordinate system with its origin at the transducer position  $x_k$ . The incident pressure  $P_{\text{inc}}(\vec{R}, \omega)$  at a general off-axis point  $Q(\vec{R})$  in far field can be found from

$$P_{\text{inc}}(\vec{R}, \omega) = -j\omega\rho v_0 a^2 \cdot \frac{\exp(-jk|\vec{R}|)}{|\vec{R}|} \cdot \frac{J_1(ka \sin \theta)}{ka \sin \theta}, \quad (6)$$

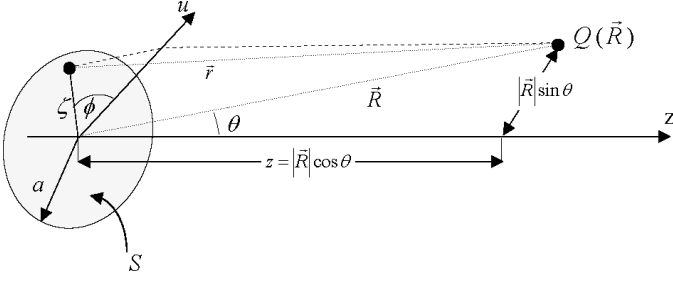


Fig. 2. Geometry for calculating the far-field response of a circular transducer.

where  $J_1$  is the first-order Bessel function,  $\rho$  denotes the specific medium density,  $v_0$  represents the normal particle velocity at the transducer's surface,  $k$  is the wave number, and  $a = d/2$  is the transducer radius [19], [20]. Eq. (6) consists of three factors: the first is a frequency dependent coefficient, the second represents a spherical wave, and the third factor, often referred to as the *jinc* function, defines the angular dependence of the amplitude of this spherical wave. The *jinc* function indicates the lobe structure of the beam in far field characterized by the main central lobe and a number of side lobes.

It is worth noting that the assumptions used by standard SAFT algorithms are valid only for small values of  $ka$  when the main lobe is wide and the amplitude of the spherical wave varies very little with the angle  $\theta$ .

The point target with an elementary surface  $s_e$  located in the point  $Q(\vec{R})$  will scatter back the incident pressure wave, and the pressure integrated over the transducer surface  $\langle P_r \rangle(\vec{R}, \omega)$  is proportional to the convolution (multiplication in frequency domain) of the incident pressure  $P_{\text{inc}}(\vec{R}, \omega)$  and the pressure reflected from the target surface  $P_{\text{ref}}(\vec{R}, \omega)$  (see [20] for details):

$$\begin{aligned} \langle P_r \rangle(\vec{R}, \omega) &= P_{\text{inc}}(\vec{R}, \omega) P_{\text{ref}}(\vec{R}, \omega) \\ &= -\frac{s_e}{2} \omega^2 (\rho v_0 a^2)^2 \frac{\exp(-j2k|\vec{R}|)}{|\vec{R}|^2} \text{jinc}^2(ka \sin \theta). \end{aligned} \quad (7)$$

Note that (7) is valid for a monostatic configuration if the transmission and reception of the transducer are separated in time and the medium is isotropic. If the transducer is modeled as a linear electromechanical system with electrical frequency responses in transmission and reception,  $H_{et}(\omega)$  and  $H_{er}(\omega)$ , respectively, the received signal will be a convolution of the incident pressure and the transducer's electrical characteristics:

$$S(\vec{R}, \omega) = H_{et}(\omega) H_{er}(\omega) \langle P_r \rangle(\vec{R}, \omega) = \langle P_r \rangle(\vec{R}, \omega) H_e(\omega), \quad (8)$$

where the joint electrical transducer frequency response is  $H_e(\omega) = H_{et}(\omega) H_{er}(\omega)$ , and it is assumed that the pulse  $u(t) = \delta(t)$  is used to excite the transducer. Finally, by inserting (7) into (8), the received signal is

$$S(\vec{R}, \omega) = \frac{s_e}{2} (\rho v_0 a^2)^2 \cdot \frac{\exp(-j2k|\vec{R}|)}{|\vec{R}|^2} \cdot \text{jinc}^2(ka \sin \theta) \cdot \omega^2 H_e(\omega) \quad (9)$$

(the minus sign was omitted; see [21] for details). The above expression is a product of four factors: the first is a constant, the second represents a spherical wave that has propagated to the target and back, the third defines the diffraction effect in the transducer's far field, and, finally, the fourth denotes the second derivative of the transducer's electromechanical transfer function.

An important consequence of (9) is that the main lobe width for a finite-sized transducer is limited by the *jinc* function, which, as mentioned above, limits the maximum length of the synthetic aperture. Verifying the above condition for a given transducer diameter  $d$ , one should keep in mind that the *jinc* has its  $-3\text{-dB}$  lobewidth  $\theta_{3\text{dB}} = 3.232/ka \cong \lambda/d$ . If  $\theta_{3\text{dB}}$  is small, maximum lengths of synthetic aperture for a given distance  $|\vec{R}| = R$  will be  $L_{\text{max}} \approx R\theta_{3\text{dB}} = R\lambda/d$ .

Below, we will confine ourselves to the targets located at the symmetry plane of the synthetic aperture, i.e., we will only consider points  $O(x, 0, z)$  at the ROI for those  $R = \sqrt{x^2 + z^2}$ . Then, assuming that distance compensation ( $1/R$ ) is performed in the receiver, we obtain after rearranging (9) the response of the transducer located at the position  $x_k$  to a single scatterer at the point  $Q(x, 0, z)$

$$\begin{aligned} S(\vec{R}, \omega) &= S(x_k, \omega) \\ &= \frac{s_e}{2} (\rho v_0 a^2)^2 \cdot \exp(-j2k\sqrt{z^2 + (x - x_k)^2}) \\ &\quad \cdot A(\omega, k_x) \cdot \omega^2 H_e(\omega), \end{aligned}$$

where  $A(\omega, k_x) = \text{jinc}^2(ak \sin \theta) = \text{jinc}^2(k_x a)$ .

To obtain a signal received by the transducer located at that point, given the real image of the point scatterers in front of the transducer  $f(x, z)$ , we have to integrate the transducer's response over the whole area:

$$\begin{aligned} S(x_k, \omega) &= \alpha \cdot A(k_x) \\ &\cdot \omega^2 H_e(\omega) \iint_{xz} f(x, z) \exp(-j2k\sqrt{z^2 + (x - x_k)^2}) dz dx, \end{aligned} \quad (10)$$

where  $\alpha$  is a constant coefficient.

To perform synthetic aperture imaging in frequency domain we need the 2D Fourier transform of the signal  $s(\vec{R}, t)$ , which means that (10) has to be further transformed from the space coordinate to spatial frequency  $k_x = k \sin \theta$  (referred to as Doppler wavenumber in sonar). It can be shown that using the principle of stationary phase [6], [7], the 1D Fourier transform of the above equation along the  $x$ -direction can be expressed as

$$S(k_x, \omega) = \alpha \cdot A(k_x) \cdot \omega^2 H_e(\omega) \cdot \int_{x,z} f(x, z) \exp\left(-j\sqrt{4k^2 - k_x^2}z\right) \exp(-jk_x x) dz dx. \quad (11)$$

If we now introduce a new set of coordinates, defined by

$$k_z(k_x) \equiv \sqrt{4k^2 - k_x^2}, \quad (12)$$

and denote  $H_{ed}(\omega) = \omega^2 H_e(\omega)$ , we can finally express  $S(k_x, \omega)$  as

$$S(k_x, \omega) = \alpha \cdot A(k_x) \cdot H_{ed}(\omega) \cdot F(k_x, k_z). \quad (13)$$

Note that now the coordinates of  $S(k_x, \omega)$  and  $A(k_x)H_{ed}(\omega)$  and those of  $F(k_x, k_z)$  are different. The coordinate transformation defined by (12), which is known as the Stolt transformation (or Stolt migration in geophysics [22]), will be denoted as  $\mathcal{S}\{\cdot\}$  in the sequel.

#### D. Imaging Algorithm

The wavenumber reconstruction algorithm presented in [7] and [15] takes the form of a spatio-temporal matched filter and the Stolt transformation that can be summarized by

$$\hat{F}(k_x, k_z) = \mathcal{S}^{-1} \left\{ \exp \left[ j \left( \sqrt{4k^2 - k_x^2} - 2k \right) r_0 \right] \cdot A^*(k_x) H_{ed}^*(\omega) S(k_x, \omega) \right\}, \quad (14)$$

where  $r_0$  is the distance to the middle of the ROI and the asterisk denotes a complex conjugate. The main function of the algorithm (14) is compensating the phase shift introduced by the imaging system (the  $\exp[\cdot]$  factor) and transforming the coordinate system (the  $\mathcal{S}^{-1}\{\cdot\}$  transform). The term  $H_{ed}^*(\omega)$  in (14) performs compression of the electrical impulse, and the term  $A^*(k_x)$  is intended to compensate the effect of angular dependence of the transducer amplitude. Since the latter is not performed satisfactorily by the matched filter (14), a modified version using a Wiener filter for the beam pattern compensation is proposed here:

$$\hat{F}(k_x, k_z) = \mathcal{S}^{-1} \left\{ \exp \left[ j \left( \sqrt{4k^2 - k_x^2} - 2k \right) r_0 \right] \cdot \frac{A^*(k_x)}{A(k_x)A^*(k_x) + \varepsilon^2} H_{ed}^*(\omega) S(k_x, \omega) \right\}. \quad (15)$$

The small constant  $\varepsilon$  should limit the filter output outside the support band of  $A(k_x)$ . There are at least two reasons why the electrical frequency response  $H_{ed}(\omega)$  is not included in the Wiener filter (14): first, it is measured separately with a limited accuracy while the  $A^*(k_x)$  is calculated analytically; second, in practical situations, the  $H_{ed}(\omega)$  will also include the space-variant low-pass effect due to the transducer spatial impulse response. Thus the filter used for the compensation of the transducer's frequency response has to be robust enough to perform well in the presence of model errors. Both practical experience

and the theoretical analysis presented in [23] show that in such situations the parameter-free matched filter (complex conjugate of the  $H_{ed}(\omega)$ ) is much more robust than the Wiener filter.

The  $\omega$ - $k$  algorithm (referred to as  $\omega$ - $k$  SAFT in the sequel) consists of three main steps:

1. 2D Fourier transform of the acquired data  $s(x_k, t) \rightarrow S(k_x, \omega)$ ,
2. Filtering and change of variables using (14) or (15), and
3. Inverse 2D Fourier transform  $\hat{F}(k_x, k_z) \rightarrow \hat{f}(x, z)$ .

The  $\omega$ - $k$  SAFT can be easily implemented and fast-executed using the existing FFT routines. It compensates for the transducer's diffraction distortion as well as for its electromechanical characteristics, which is a great advantage in contrast to the t-d SAFT based on DAS operations. Note, however, that the above applied transducer model is valid in far field only, and in the near field the low-pass filtering effect due to the finite lengths of the transducer's SIRs must also be compensated [3].

Although the  $\omega$ - $k$  SAFT was derived above for the monostatic configuration, the extension to a bistatic or multistatic setup is quite straightforward and consists of modifying the imaging system model starting from (7) where different sound paths are to be accounted for. This finally results in a modified phase compensation term in (14) and (15).

The main disadvantage of the  $\omega$ - $k$  algorithms is the need to interpolate from one 2D sampling grid to another grid defined by the Stolt transformation. Indeed, by virtue of physics, ultrasonic data acquired by a transducer correspond to a curved surface while the real image traditionally is reconstructed in a rectangular grid.

Below, we illustrate the performance of the  $\omega$ - $k$  SAFT using simulations and we compare it to that of the standard t-d SAFT.

### III. SIMULATIONS

The simulations were performed for the synthetic aperture created from the measurements made by circular transducers with various diameters  $d$  for a point target located in water at different distances  $z_t$  from the aperture. Time-domain simulations were used and the spatial impulse responses of circular transducers in the simulations were calculated from analytical solutions [24]. Standard pixel-driven t-d SAFT implementation was used in the simulations. In this implementation the theoretical hyperbolas (binary patterns) corresponding to the respective ranges are shifted across the processed RF 2D data, and the values of pixels where the hyperbola crossed the data are summed. A linear interpolation was used to compensate the effects of discretization. This implementation can be thought of as a spatially variant matched filter employing the theoretical response of the point target received by a point transducer with an unlimited bandwidth. The output of the matched filter applied to a real RF ultrasonic

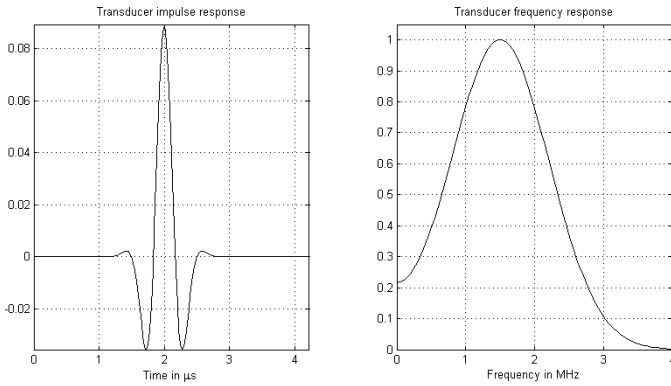


Fig. 3. Exciting pulse used in simulations, and its Fourier transform.

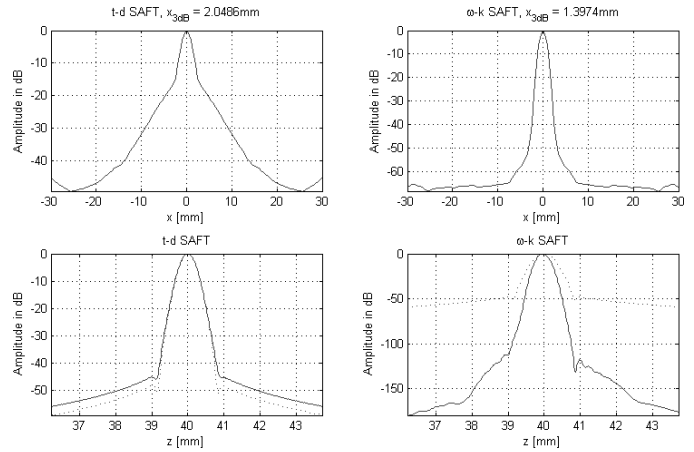


Fig. 5. Beam projections obtained from B-scans shown in Fig. 4 in decibels. Upper: lateral profile obtained from the t-d SAFT (left) and the  $\omega$ - $k$  SAFT (right). Note the values of 3-dB resolution (beam width) printed above the respective panels. Lower: envelope of the center A-scan at  $x = 0$  in the B-scan obtained from the t-d SAFT (left) and the  $\omega$ - $k$  SAFT (right). The dotted line represents the envelope of the original A-scan (raw data).

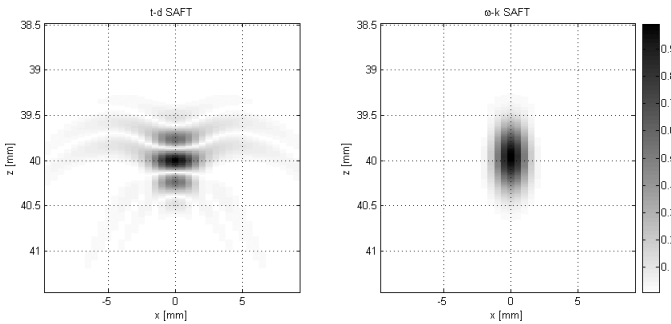


Fig. 4. Plots of the normalized amplitudes obtained for the point target located at distance 40 mm from aperture after processing with the t-d SAFT (left) and the  $\omega$ - $k$  SAFT (right). Note that the absolute value of the t-d SAFT result is presented.

signal, due to the oscillatory character of the transducer response, can take both positive and negative values.

The  $\omega$ - $k$  SAFT was implemented according to (15), which means that the beam pattern compensation was used in all results presented below, except Fig. 8, for comparing the resolution of different algorithms. Contrary to the t-d SAFT, which processed RF signals, the  $\omega$ - $k$  SAFT was implemented on complex-valued quadrature demodulated signals. To facilitate comparisons with the  $\omega$ - $k$  SAFT, the envelopes (calculated using Hilbert transform) of the t-d SAFT results are presented in figures below, except Figs. 4 and 10, where the rectified amplitudes are presented. The lateral resolution of both algorithms is compared using projection of the cross-range beam profiles on the transducer plane (the  $xy$  plane). The range resolution is illustrated by the envelopes of the center A-scans at  $x = 0$  in the B-scans.

The apertures used for the t-d SAFT included the number of elements calculated for each target distance and each transducer diameter according to (2), given a constant pitch  $\Delta_x \leq (d/4)$ . The transducers were excited by the broadband pulse shown in Fig. 3, with its center frequency at 1.5 MHz.

The first simulation shown in Figs. 4 and 5 was performed for a circular transducer with diameter 4 mm and a point target located at 40 mm. The aperture used for the t-d SAFT consisted of 20 elements, spatial sampling

was 0.5 mm, and the proposed  $\omega$ - $k$  SAFT processed the ROI  $x \in [-30, 30]$ ;  $z \in [25, 55]$  (only a small center part of the ROI is shown in Fig. 4). In Figs. 4 and 5 it can be seen that the lateral resolution of the  $\omega$ - $k$  SAFT is much better than that of the t-d SAFT (the  $-3$ -dB beam profile widths  $x_{3dB}$  evaluated using interpolation with second order polynomial were, respectively, 1.4 mm and 2.0 mm). The  $\omega$ - $k$  SAFT profile has its side lobes at the level less than  $-60$  dB, while the t-d SAFT profile is characterized by the broad side artifacts seen in Fig. 4 and clearly pronounced as a broad lobe in Fig. 5 (upper part).

The temporal resolution of both algorithms can be evaluated from the lower part of Fig. 5 where envelopes of A-scans at  $x = 0$  in the respective B-scans are plotted for the t-d SAFT and the  $\omega$ - $k$  SAFT (the corresponding A-scan profile from the raw data is also plotted as a reference). It is apparent that the  $\omega$ - $k$  SAFT results in a much better temporal resolution than that obtained from the t-d SAFT. In Fig. 5 it can be seen that the range profile obtained from the t-d SAFT has essentially the same width as the raw data, while the  $\omega$ - $k$  SAFT yields a much smaller profile decreasing to approximately  $-120$  dB.

To evaluate robustness of both algorithms in the presence of measurement noise, the same experiment was repeated again but white zero-mean Gaussian noise was added to the (raw) simulated data. The profiles presented in Fig. 6 show that the lateral profile width  $x_{3dB}$  is essentially unchanged and the ratio of the main lobe amplitude to the noise level is similar for both algorithms, approximately 25 dB (for the corresponding noise ratio approximately 20 dB in the raw data). The range profile for the  $\omega$ - $k$  SAFT is much better than that for the t-d SAFT. The maximum signal-to-noise ratio is approximately 30 dB higher.

The lateral resolution of both algorithms for different transducer sizes (but the same electrical impulse response

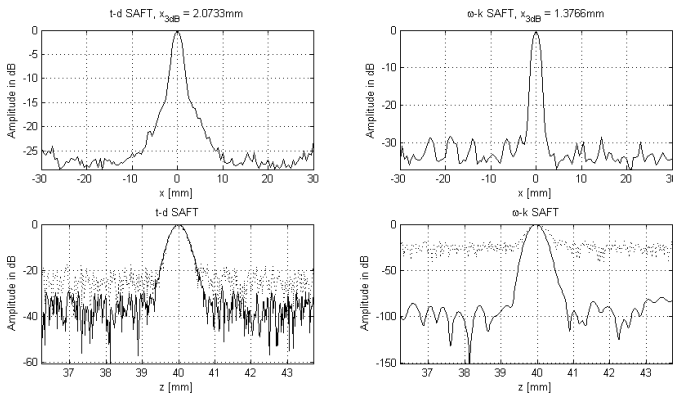


Fig. 6. Beam projections obtained after processing simulated data from the same setup as that in Fig. 5, but corrupted by Gaussian noise. Upper: lateral profile obtained from the t-d SAFT (left) and the  $\omega$ - $k$  SAFT (right). Note printed values of  $x_{3dB}$  (3-dB beam width) as a measure of resolution. Lower envelope of the center A-scan at  $x = 0$  in the B-scan obtained from the t-d SAFT (left) and the  $\omega$ - $k$  SAFT (right); dotted line represents the original B-scan profile (raw data).

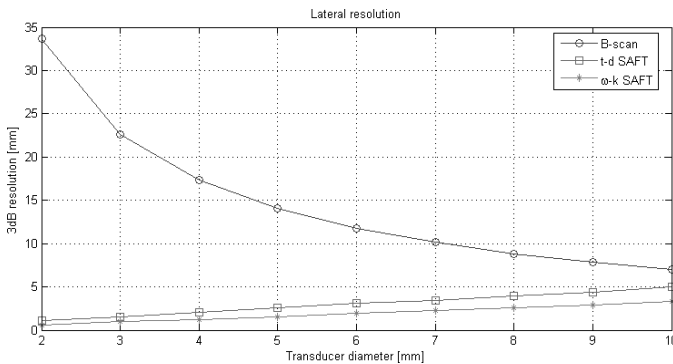


Fig. 7. Lateral resolution (the  $x_{3dB}$ ) as a function of transducer diameter for the t-d SAFT and the  $\omega$ - $k$  SAFT for target distance 100 mm. The 3-dB profile width of the ultrasonic data (B-scan) is plotted for reference.

shown in Fig. 3) for a target located at a distance 100 mm can be compared in Fig. 7 (the  $-3$ -dB profile width of the raw B-scan is plotted as a reference). In Fig. 7 it can be seen that the resolution of both algorithms decreases proportionally (the  $x_{3dB}$  increases) to the transducer diameter. However, the  $\omega$ - $k$  SAFT has the superior resolution, which is better than that predicted by (3).

For large transducer diameters,  $d > 10$  mm for the distance 100 mm shown in Fig. 7, the application of the synthetic aperture does not yield improvements in resolution. It is apparent that for large transducers, as the angular information in the target response decreases, the use of t-d SAFT algorithms does not result in significant improvement of resolution. In other words, the transducer lobe becomes so narrow that processing consecutive A-scans does not improve the lateral resolution. Note that this is a direct proof of the general rule according to which synthetic aperture can be effective only if the point source assumption is fulfilled.

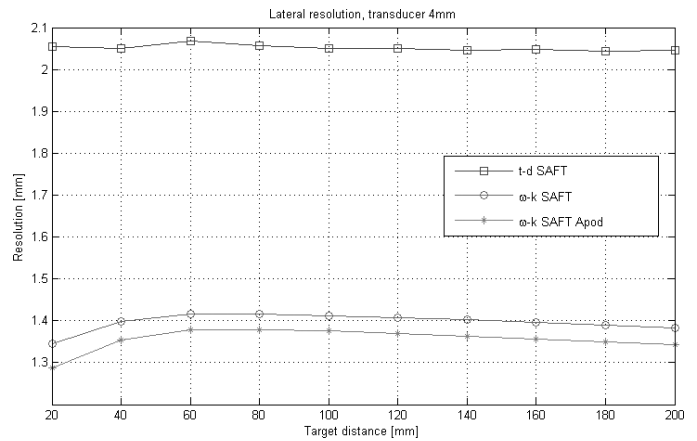


Fig. 8. Lateral resolution in terms of the profile width  $x_{3dB}$  as a function of target distance for the t-d SAFT and the  $\omega$ - $k$  SAFT, respectively, without and with aperture compensation for transducer diameter  $d = 4$  mm.

In Fig. 8, the resolution obtained with the t-d SAFT and the  $\omega$ - $k$  SAFT is presented as a function of target distance for transducer diameter  $d = 4$  mm. The results obtained for the  $\omega$ - $k$  SAFT without aperture compensation (14) are plotted beside those obtained for the proposed algorithm with Wiener filter (15). All three algorithms keep approximately constant resolution  $x_{3dB}$  as predicted by (3). However, while the resolution of the t-d SAFT is approximately equal to  $d/2$ , the resolution of the  $\omega$ - $k$  SAFT is higher (smaller  $x_{3dB}$ ). The difference between t-d SAFT and  $\omega$ - $k$  SAFT implementation is approximately 30% (taking the t-d SAFT's resolution as a reference). The effect of beam pattern compensation using a Wiener filter (15) is clearly pronounced; the respective  $x_{3dB}$  of the  $\omega$ - $k$  SAFT with compensation is approximately 5% smaller for all distances.

Summarizing, the simulations have shown that the  $\omega$ - $k$  SAFT offers a clear performance improvement compared with the t-d SAFT in terms of resolution and lower side lobes. An additional improvement is obtained by introducing beam pattern compensation in the  $\omega$ - $k$  SAFT (15).

#### IV. EXPERIMENT

To verify the performance of the compared algorithms, a simple experiment was carried out in a water tank. The measurements were performed using a planar 0.375-inch 2.25-MHz immersion transducer V325-SU from Panametrics (Waltham, MA). Three steel wires of diameter 0.2 mm, immersed in water at distances  $z_t = 221, 251,$  and 280 mm from the aperture were used as targets. The transducer was moved in 1-mm steps and the ultrasonic data were acquired with sampling frequency 80 MHz and digitized using an 8-bit AD converter.

The experimental setup was simulated using the software tools used for the simulations presented in the preceding section. The simulation results are summarized in Fig. 9, where lateral profiles are presented in the upper

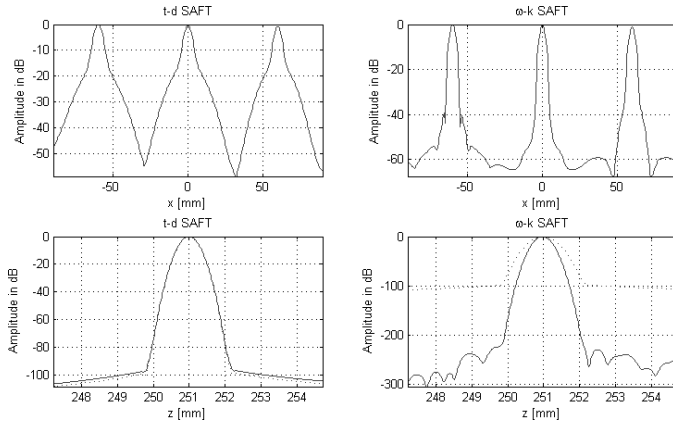


Fig. 9. Simulation results obtained in the experimental setup for three targets spaced 30 mm from each other (the middle target at the distance 251 mm from SA). Upper panel: lateral profile obtained using the t-d SAFT (left) and the  $\omega$ - $k$  SAFT with lobe compensation (right). Lower panel: range profiles obtained for the middle target using the t-d SAFT (left) and the  $\omega$ - $k$  SAFT (right); dotted line represents the original B-scan profile (raw data).

panels and the temporal resolution is illustrated by the graphs in the lower panel. The lateral resolution  $x_{3dB}$  estimated using interpolation of profiles with the second order polynomial was 4.9 mm for the t-d SAFT and 3.3 mm for the  $\omega$ - $k$  SAFT with lobe compensation. The resolution was similar for all three targets spaced 30 mm from each other. The side lobe level was  $-20$  dB for the t-d SAFT and  $-40$  dB for the  $\omega$ - $k$  SAFT. Also, the temporal resolution of the  $\omega$ - $k$  SAFT was much better than that of the t-d SAFT (cf. lower panel of Fig. 9).

The results obtained from the ultrasonic measurements performed in the simulated setup are presented in Fig. 10. The B-scans and lateral profiles are shown respectively left and right for raw data (upper panel), the t-d SAFT-processed data (middle panel), and the data processed using the  $\omega$ - $k$  SAFT with lobe amplitude compensation (lower panel). Amplitudes of the raw data were distance-compensated after the acquisition. Both the t-d SAFT and the  $\omega$ - $k$  SAFT yield clear improvement of the lateral resolution; the values estimated in the same way as in the simulations are 4.6 mm for the t-d SAFT and 3.6 mm for the  $\omega$ - $k$  SAFT. Both values are very close to those obtained in simulations. The t-d SAFT has well pronounced side lobes both at the B-scan and at the cross-range profile at the level of  $-15$  dB. The side lobes of the  $\omega$ - $k$  SAFT cannot be seen in the B-scan with linear amplitude coding, but the corresponding value read out of the profile is approximately  $-32$  dB. The amplitudes of all targets are well preserved both by the t-d SAFT and by the  $\omega$ - $k$  SAFT.

The origin of the side lobes present in the t-d SAFT imaging can be understood if the responses in the t-d SAFT imaging result, shown in Figs. 4 and 10, are analyzed more closely. It can be seen that the main lobe corresponding to each target has a kind of “wings” at both its sides. The “wings” originate from the simplified implementation of the t-d SAFT, which does not account for

the transducer electrical impulse response. Indeed, when a single pixel-thick hyperbola is shifted across the processed B-scan (see the description of the t-d SAFT implementation in the introduction to Section III), a number of overlapping points will be detected due to the finite width of the transducer response, and this effect is particularly well pronounced in the neighborhood of the main peak corresponding to the target position. The  $\omega$ - $k$  SAFT does not have this drawback since the transducer’s electrical frequency response is included in the model of the imaging setup.

In summary, the experimental result is in good agreement with the simulated one, and it confirms the superior performance of the proposed  $\omega$ - $k$  SAFT.

## V. CONCLUSIONS

The  $\omega$ - $k$  SAFT for synthetic aperture imaging proposed in the paper is based on the frequency domain model of the imaging system. The algorithm performs the 2D FFT transform of the measured ultrasonic data followed by the 2D matched filter and the Stolt transformation. The result is transformed back to time-space domain using the inverse FFT. A Wiener filter based on the far-field model of the transducer beam pattern is proposed for the compensation of the main lobe amplitude variation.

The simulated results revealed that the  $\omega$ - $k$  SAFT offers a clear performance improvement compared with the standard time-domain SAFT in terms of both improved range resolution and lateral resolution as well as lower side lobes in the images of point targets. The lateral resolution of the  $\omega$ - $k$  SAFT in a wide range of target distances is approximately 30% better than the theoretical limit equal to half diameter of the transducer used in the synthetic aperture.

The transducer beam pattern compensation based on the Wiener filter concept yields a clear improvement of the lateral resolution, constant for all target distances.

The monostatic configuration presented in the paper can easily be replaced by a bistatic or multistatic setup. Similarly, the transducer model, derived here for the circular sources, can easily be generalized to other transducer geometries, for instance, rectangular array elements. When doing so, one should bear in mind, however, that SAFT requires half of the pitch used in conventional array systems.

## ACKNOWLEDGMENT

The author gratefully acknowledges helpful discussions with Dr. Tomas Olofsson from Uppsala University.

## REFERENCES

- [1] J. A. Seydel, “Ultrasonic synthetic-aperture focusing techniques,” in *NDT Research Techniques for Nondestructive Testing*. New York: Academic Press, 1982.



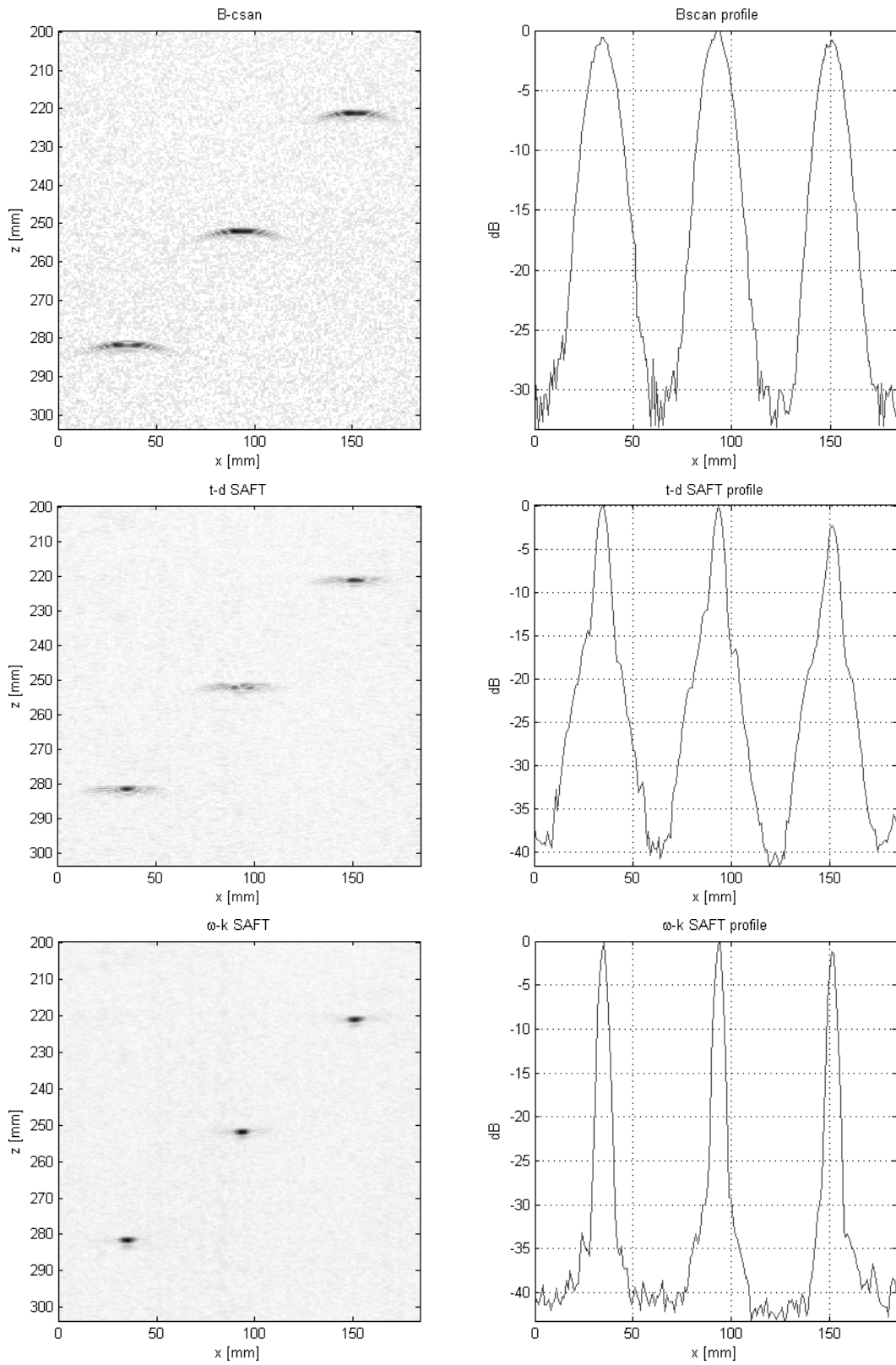


Fig. 10. Results obtained in the experimental setup for three immersed targets spaced 30 mm in range (the middle target at the distance 251 mm from the SA). Upper panel: B-scan (left) and lateral profile obtained from raw data (right). Middle panel: B-scan (left) and the lateral profile obtained using the t-d SAFT (right). Lower panel: B-scan (left) and the lateral profile obtained for the  $\omega$ -k SAFT with lobe compensation (right). Note that the B-scans of raw data and the t-d SAFT result are rectified. For better presentation of the background noise level, pixel amplitude in the B-scan images was compressed using a square root function.

- [2] V. Schmitz, S. Chalkov, and W. Muller, "Experience with synthetic aperture focusing technique in the field," *Ultrasonics*, vol. 38, pp. 731–738, 2000.
- [3] F. Lingvall, T. Olofsson, and T. Stepinski, "Synthetic aperture imaging using sources with finite aperture-deconvolution of the spatial impulse response," *J. Acoust. Soc. Amer.*, vol. 114, pp. 225–234, 2003.
- [4] S. R. Doctor, T. E. Hall, and L. D. Reid, "SAFT—the evolution of a signal processing technology for ultrasonic testing," *NDT International*, vol. 19, pp. 163–167, June 1986.
- [5] M. Karaman, P.-C. Li, and M. O'Donnell, "Synthetic aperture imaging for small scale systems," *IEEE Trans. Ultrason., Ferroelect., Freq. Contr.*, vol. 42, no. 3, pp. 429–442, May 1995.
- [6] M. Soumekh, "Reconnaissance with ultra wideband UHF synthetic aperture radar," *IEEE Signal Processing Mag.*, vol. 12, no. 4, pp. 21–40, July 1995.
- [7] P. T. Gough and D. W. Hawkins, "Unified framework for modern synthetic aperture imaging algorithms," *Int. J. Imag. Syst. Technol.*, vol. 8, pp. 343–358, 1997.
- [8] L. J. Busse, "Three-dimensional imaging using a frequency-domain synthetic aperture focusing technique," *IEEE Trans. Ultrason., Ferroelect., Freq. Contr.*, vol. UFFC-39, no. 2, pp. 174–179, Mar. 1992.
- [9] D. Vray, C. Haas, T. Rastello, M. Krueger, E. Brusseau, K. Schroeder, G. Gimenez, and H. Ermert, "Synthetic aperture-based beam compression for intravascular ultrasound imaging," *IEEE Trans. Ultrason., Ferroelect., Freq. Contr.*, vol. 48, no. 1, pp. 189–201, Jan. 2001.
- [10] J. Ylitalo and H. Ermert, "Ultrasound synthetic aperture imaging: Monostatic approach," *IEEE Trans. Ultrason., Ferroelect., Freq. Contr.*, vol. 41, no. 3, pp. 333–339, May 1994.
- [11] M. O'Donnell, M. Eberle, D. Stephens, J. Litzza, K. San Vicente, and B. M. Shapo, "Synthetic phased arrays for intraluminal imaging of coronary arteries," *IEEE Trans. Ultrason., Ferroelect., Freq. Contr.*, vol. 44, no. 3, pp. 714–721, May 1997.
- [12] C. Frazier, N. Cadalli, D. Munson, Jr., and W. O'Brien, "Acoustic imaging of objects buried in soil," *J. Acoust. Soc. Amer.*, vol. 108, no. 1, pp. 147–156, 2000.
- [13] E. Biagi, N. Dreoni, L. Masotti, I. Rossi, and M. Scabia, "ICARUS: Imaging pulse compression algorithm through remapping of ultrasound," *IEEE Trans. Ultrason., Ferroelect., Freq. Contr.*, vol. 52, no. 2, pp. 261–278, Feb. 2005.
- [14] D. C. Munson, Jr., J. D. O'Brien, and W. K. Jenkins, "A tomographic formulation of spotlight-mode synthetic aperture radar," *Proc. IEEE*, vol. 71, no. 8, pp. 917–925, Aug. 1983.
- [15] R. Bamler, "A comparison of range-Doppler and wavenumber domain SAR focusing algorithms," *IEEE Trans. Geosci. Remote Sensing*, vol. 30, pp. 706–713, 1992.
- [16] P. T. Gough and D. W. Hawkins, "Imaging algorithms for a strip-map synthetic aperture sonar: Minimizing the effects of aperture errors and aperture undersampling," *IEEE Trans. Oceanic Eng.*, vol. 22, pp. 27–39, 1997.
- [17] L. J. Cutrona, "Comparison of sonar system performance achievable using synthetic-aperture techniques with the performance achievable by more conventional means," *J. Acoust. Soc. Amer.*, vol. 58, no. 2, pp. 336–348, 1975.
- [18] M. Soumekh, *Synthetic Aperture Radar Signal Processing*. New York: Wiley, 1999.
- [19] G. S. Kino, *Acoustic Waves: Devices, Imaging and Analog Signal Processing*. Englewood Cliffs, NJ: Prentice-Hall, 1987.
- [20] L. Schmerr, *Fundamentals of Ultrasonic Nondestructive Evaluation: A Modeling Approach*. New York: Kluwer Academic/Plenum Publishers, 1998.
- [21] A. Lhémery, "Impulse-response method to predict echoes from targets of complex geometry. Part I: Theory," *J. Acoust. Soc. Amer.*, vol. 90, no. 5, pp. 2799–2807, Nov. 1991.
- [22] R. H. Stolt, "Migration by Fourier transform," *Geophysics*, vol. 43, pp. 23–48, 1978.
- [23] F. Lingvall, "Time-domain reconstruction methods for ultrasonic array imaging," Ph.D. dissertation, Dept. of Engineering Sciences, Uppsala University, Uppsala, Sweden, 2004.
- [24] P. R. Stephanishen, "Transient radiation from pistons in a rigid infinite planar baffle," *J. Acoust. Soc. Amer.*, vol. 49, pp. 1627–1638, 1971.



**Tadeusz Stepinski** was born in December 1950 in Poland. He obtained his M.Sc. degree in electrical engineering from the Technical University of Szczecin, Poland, and Ph.D. degree in technology from the Technical University of Warsaw, Poland, in 1973 and 1983, respectively.

From 1973 to 1984 he was with the Institute of Industrial Automation at the Department of Electrical Engineering of the Technical University of Szczecin, Poland, where he served as teaching assistant, teaching courses

on the subjects of systems identification and modeling, automatic control, industrial control systems, and electronic circuits.

From 1984 to 1988 he was with the Swedish company AB Sandvik Bergstrand where he became actively involved in R&D in the field of nondestructive evaluation (NDE).

Since 1988 he has been with Signals and Systems at Uppsala University, Sweden. He initiated research activity in the field of NDE at Uppsala University. His research is focused on the application of modern signal processing to NDE. His research interests are in the areas of ultrasonics, array processing, digital signal processing, and measurement engineering. He also has served as a lecturer, teaching courses for undergraduate students on the subjects of signal processing, NDE, virtual measurement systems, and sensors.

In 2002 he was appointed full Professor in Electrical Measurement Engineering at Uppsala University. He is author and co-author of more than 100 journal and conference papers and reports.

Dr. Stepinski is a Senior Member of IEEE, member of Acoustical Society of America, ASNT (American Society for NDT), and the British Institute of Non-Destructive Testing. He chairs the Committee for New Techniques and Development in FOP (the Swedish Society for NDE).